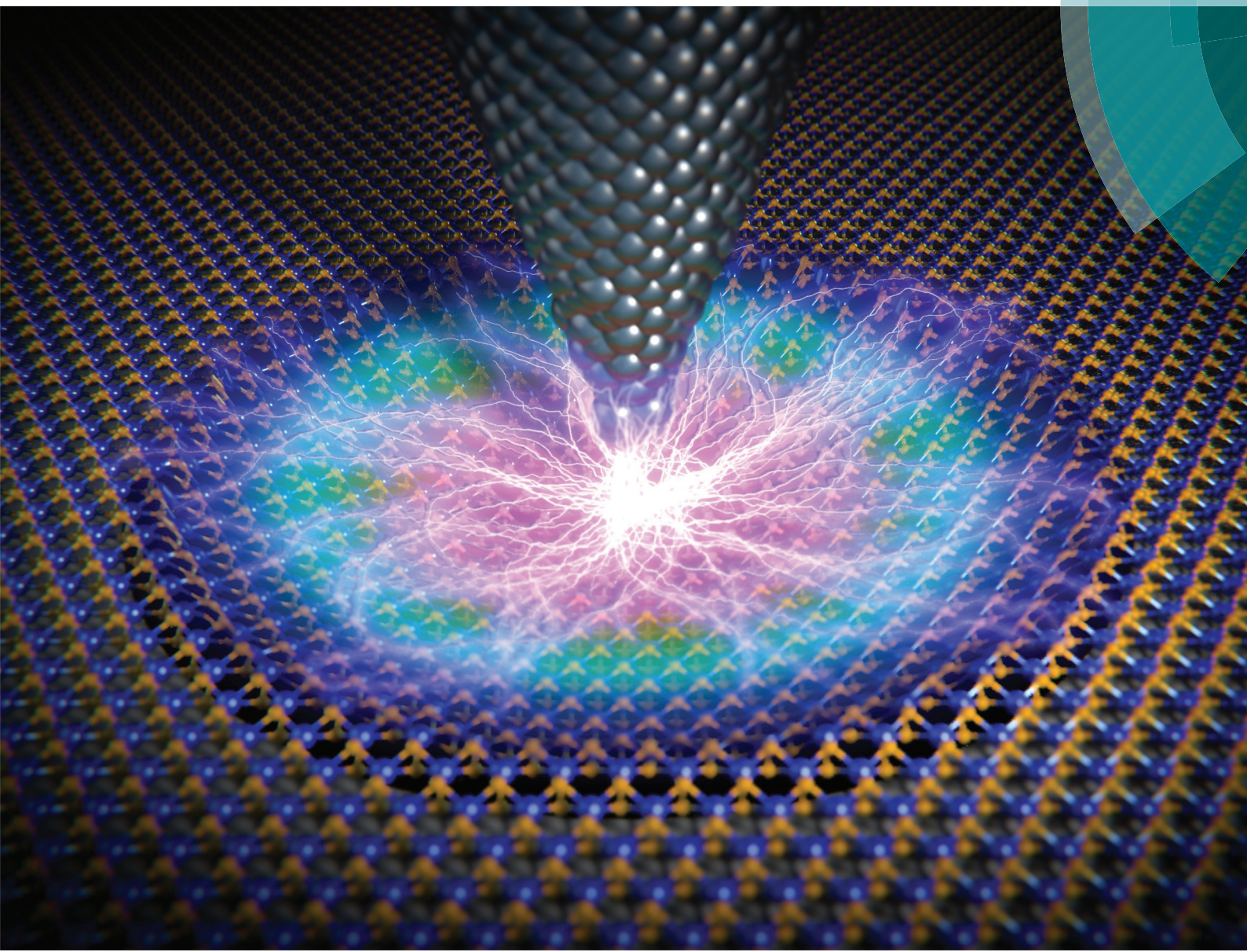


Nanoscale

rsc.li/nanoscale



ISSN 2040-3372



COMMUNICATION

Mario Lanza *et al.*

Enhanced piezoelectric effect at the edges of stepped molybdenum disulfide nanosheets





Cite this: *Nanoscale*, 2017, **9**, 6237

Received 29th November 2016,
Accepted 21st February 2017

DOI: 10.1039/c6nr09275f
rsc.li/nanoscale

Enhanced piezoelectric effect at the edges of stepped molybdenum disulfide nanosheets[†]

Xiaoxue Song,^a Fei Hui,^a Keith Gilmore,^b Bingru Wang,^a Guangyin Jing,^c Zhongchao Fan,^d Enric Grustan-Gutierrez,^a Yuanyuan Shi,^a Lucia Lombardi,^e Stephen A. Hodge,^e Andrea C. Ferrari^e and Mario Lanza^{*a}

The development of piezoelectric layered materials may be one of the key elements enabling expansion of nanotechnology, as they offer a solution for the construction of efficient transducers for a wide range of applications, including self-powered devices. Here, we investigate the piezoelectric effect in multilayer (ML) stepped MoS₂ flakes obtained by liquid-phase exfoliation, which is especially interesting because it may allow the scalable fabrication of electronic devices using large area deposition techniques (e.g. solution casting, spray coating, inkjet printing). By using a conductive atomic force microscope we map the piezoelectricity of the MoS₂ flakes at the nanoscale. Our experiments demonstrate the presence of electrical current densities above 100 A cm⁻² when the flakes are strained in the absence of bias, and the current increases proportional to the bias. Simultaneously collected topographic and current maps demonstrate that the edges of stepped ML MoS₂ flakes promote the piezoelectric effect, where the largest currents are observed. Density functional theory calculations are consistent with the ring-like piezoelectric potential generated when the flakes are strained, as well as the enhanced piezoelectric effect at edges. Our results pave the way to the design of piezoelectric devices using layered materials.

Piezoelectricity is the property of a material to convert mechanical energy into electrical energy and *vice versa*.¹ The piezoelectric effect appears when the atomic symmetry of a material is broken due to an external mechanical stress,² causing the

accumulation of electric charges.² If a load resistor is connected, the device can produce a net current.³ This effect has been used in a wide range of applications, including sensors,⁴ detectors,⁵ transducers⁶ and energy harvesters.⁷ With the rise of low dimensional materials, the interest in piezoelectric devices has increased considerably, as it is expected to be enhanced with reduced dimensionality.⁸ During the last decade, zinc oxide (ZnO) nanowires have been the most studied piezoelectric nanomaterials,^{9–11} and it has been reported that they are able to generate large current densities (*J*) above 1 A cm⁻²,¹² significantly larger than those thus far observed in other clean energy technologies, such as solar cells (~30 mA cm⁻²).¹³ The presence of piezoelectricity in other low dimensional materials, such as layered materials (LMs), such as hexagonal boron nitride (*h*-BN),¹⁴ doped graphene (with Li, K, H or F),^{15,16} or transition metal dichalcogenides (TMDs),^{17–20} is even more desirable, since they can provide additional properties, such as large mechanical strength, transparency and high chemical stability.^{21,22}

The existence of piezoelectricity in LMs was theoretically suggested in ref. 14, where it was calculated that ML-*h*-BN with an odd number of layers (*N*) shows a piezoelectric effect, with the intensity inversely proportional to *n*. Ref. 15, based on density functional theory (DFT) calculations, suggested that graphene (which is not inherently piezoelectric,²³) may show a small ($e_{11} = 0.5 \times 10^{-10}$ C m⁻¹) out-of-plane piezoelectric response by placing impurities (such as K, H, F and/or Li) on one face. Also using computational methods, ref. 16 reported that graphene may show an even larger ($e_{11} = 4.5 \times 10^{-10}$ C m⁻¹) piezoelectric effect in-plane, if its point group symmetry is altered with B or N dopants. Piezoelectricity was also theoretically predicted in TMDs, including MoS₂, MoSe₂, MoTe₂, WS₂, WSe₂, and WTe₂,¹⁷ with MoS₂ having the largest piezoelectric coefficient ($e_{11} = 2.9 \times 10^{-10}$ C m⁻¹).¹⁸ MoS₂ is also the only TMD in which piezoelectricity has been experimentally verified. Ref. 19 used a programmable electrometer to monitor the voltages generated by mechanically exfoliated MoS₂ flakes (with *N* = 1–6) when exposed to in-plane mechanical strains. Ref. 20 used an atomic force microscope (AFM) to detect the

^aInstitute of Functional Nano & Soft Materials (FUNSOM), Collaborative Innovation Center of Suzhou Nanoscience and Technology, Soochow University, 199 Ren-Ai Road, Suzhou, 215123, China. E-mail: mlanza@suda.edu.cn

^bEuropean Synchrotron Radiation Facility, BP 220 38047 Grenoble, Cedex, France

^cState Key Lab Incubation Base of Photoelectric Technology and Functional Materials, School of Physics, Northwest University, 229 Taibai Beilu, Xi'an, 710069, China

^dEngineering Research Center for Semiconductor Integrated Technology, Institute of Semiconductors, Chinese Academy of Sciences, Beijing 100083, China

^eCambridge Graphene Centre, University of Cambridge, 9 JJ Thomson Ave, Cambridge, CB3 0FA, UK

[†]Electronic supplementary information (ESI) available. See DOI: [10.1039/c6nr09275f](https://doi.org/10.1039/c6nr09275f)

deflection of suspended 1 to 3 layers thick MoS₂ flakes (obtained by mechanical exfoliation) when subjected to different bias conditions. Ref. 3 and 20 further corroborated these observations, identifying MoS₂ as the most promising piezoelectric LM. However, mechanically exfoliated MoS₂^{18,19} is not suited to large scale device fabrication,²⁴ as the size of the flakes used thus far is too small (just hundreds of nanometers, while wafer scale sizes are preferred), plus they often show thickness fluctuations. Chemical vapor deposition (CVD) has been used to grow triangular monolayer MoS₂ (1L-MoS₂) flakes with sizes of ~6 μm,³ but the electrodes must be *in situ* patterned at specific locations (at the edges of the MoS₂ flakes) by electron beam lithography, which is not easily scalable. To the best of our knowledge, the presence of piezoelectricity in MoS₂ flakes obtained using liquid-phase exfoliation (LPE)^{25–27} has not been reported. Moreover, while ref. 3, 18 and 20 investigated the presence of piezoelectricity in MoS₂ at the nanoscale using an AFM, we are not aware of any work reporting nanoscale mapping of the piezoelectric effect.

Here we map piezoelectricity in MoS₂ flakes at the nanoscale using a conductive atomic force microscope (CAFM). Stepped (pyramidal) ML-MoS₂ flakes produced by LPE^{25–27} are deposited on a silicon substrate with holes, and the suspended membranes are scanned with the tip of a CAFM using different contact forces. In the absence of bias, electrical currents up to ~100 pA appear ($J = 100 \text{ A cm}^{-2}$), and they increase with the contact force. Current maps with sizes down to

250 nm × 250 nm reveal that the MoS₂ edges generate piezo-electric currents much larger than any other features in the sample. The scalability of LPE is an important step towards the use of this material in large area printed electronics,²⁸ for applications such as self-powered devices,²⁸ piezoelectric transformers,²⁹ and antennas.³⁰

The MoS₂ ink is prepared by dispersing 4 mg of MoS₂ powder (purchased from Alfa Aesar) in 10 mL isopropyl alcohol (IPA) using an ultrasonic bath (KQ-100KDB High Power NC, Kunshan Ultrasonic Instruments) at a power of 90 W for 26 hours. The thin flakes and the larger particles are separated using a H1650 W centrifuge (from Cence Instrument) working at 4000 rpm (2500g) for 15 minutes, which forms a supernatant containing thin MoS₂ flakes (Fig. 1a). For characterization and device fabrication, only the supernatant is utilized.

The MoS₂ ink (Fig. 1a) is drop-cast onto an n⁺-Si wafer substrate and allowed to dry naturally for 5 hours. Scanning electron microscopy (SEM) shows that the substrate is almost completely covered with MoS₂ flakes (Fig. 1b). The flakes exhibit squared/rhomboid shapes with an average lateral size of 6.67 μm ± 2.38 μm, as corroborated by statistically analyzing more than 1000 flakes (see Fig. S1 in the ESI†). This large size (compared to other studies²⁵ and commercially available products³¹) may be related to the low power used during the ultrasonication step, which is able to overcome the inter-layer van der Waals forces but not sufficient to significantly disrupt the

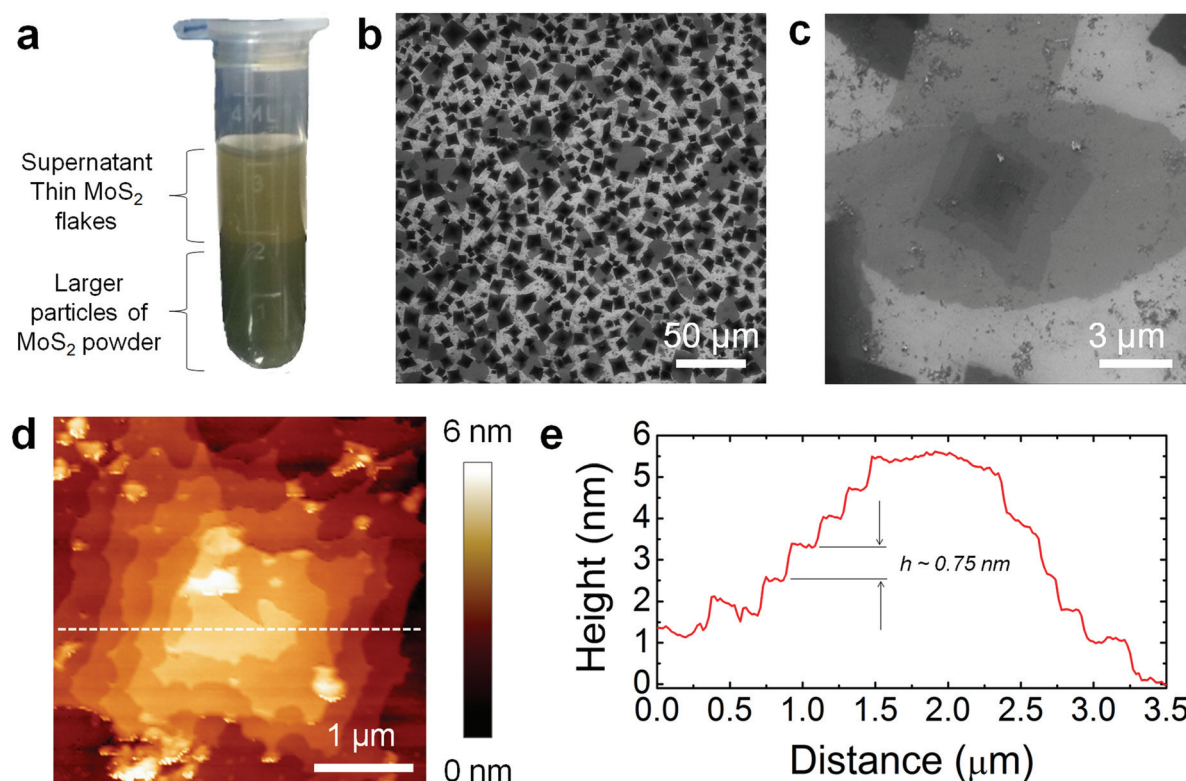


Fig. 1 (a) Piezoelectric ink made from liquid-phase exfoliated MoS₂. (b) and (c) SEM images of stepped ML-MoS₂ flakes. (d) Topographic AFM image of a ML stepped MoS₂ flake. (e) Topographic cross section highlighted in (d) with a dashed line.

in-plane covalent framework.³² High resolution SEM images reveal the stepped nature of the ML-MoS₂ flakes (Fig. 1c). The morphology of the flakes is further characterized by means of topographic AFM maps in tapping mode (Fig. 1d). The stepped nature of the flakes can be seen in the cross section (see Fig. 1e). The typical thickness of the flakes is between 5 and 15 nm, and the height of the steps measured in Fig. 1e is ~ 0.75 nm. While the ideal thickness of a MoS₂ layer is 0.65 nm,³³ it has been reported that AFM measurements show wider distributions in heights (between 0.6 and 0.9 nm)³⁴ due to the presence of adsorbates or other interactions between the film and oxide substrate surface.³⁵ Hence, we assume each step in Fig. 1e to correspond to a 1L-MoS₂. Thus, our typical MoS₂ flakes have $N = 7\text{--}20$. The Raman spectrum in Fig. S2† shows the two fingerprints of (2H) MoS₂ at 383 cm^{-1} and at 409 cm^{-1} corresponding to the E¹_{2g} and A_{1g} modes, respectively.³⁶ Considering the spectral distance between the E¹_{2g} and A_{1g} peaks we conclude that the MoS₂ dispersion predominantly consists of flakes with $N > 6$.

The flakes are also deposited on an n⁺⁺-Si substrate with holes (see Fig. S3 in the ESI†) following the same procedure. Fig. 2a shows the SEM image of one such hole before depositing the MoS₂ flakes. Fig. 2b shows holes partially and fully covered with flakes. Fig. 2d and e plot the topographic AFM maps collected on uncovered and covered holes. The presence of a MoS₂ flake blocks the penetration of the tip into the $2.2\text{ }\mu\text{m}$ deep hole, as depicted by the cross sections in Fig. 2f. Another factor that corroborates the presence of MoS₂ on the hole is the shape of force-distance (F-d) curves. Fig. 2c plots the typical F-d curves collected on both the suspended MoS₂

membrane and on Si (red and blue spots in Fig. 2b, respectively). The F-d curve on Si shows the adhesion peak typically observed on rigid materials,³⁷ manifested as a large negative peak in the retrace curve. On the contrary, the shape of the F-d curve on the MoS₂ flakes points to progressive attachment and detachment, a behavior characteristic of suspended membranes.²⁰ These results confirm that the MoS₂ flakes successfully cover the holes.

The suspended MoS₂ flakes can be strained by increasing the contact force during the topographic AFM scan. In order to better understand the relationship between force and flake deformation, we measure sequences of topographic maps in contact mode by applying different vertical forces with the AFM tip (from 0 to 45 nN). The AFM maps and their cross sections (Fig. 3) reveal a progressive increase of the depth with the applied contact force. The asymmetric shape of the cross-sections at low contact forces is related to the direction of the scan, as indicated in Fig. S4 in the ESI.† From Fig. 3, some conclusions can be extracted: (i) in all cases the depths are much smaller than the depth of the hole (see Fig. 2f for comparison) corroborating that the shapes observed are related to the morphology of the suspended flakes, not to the shape of the hole; (ii) the experiment is repeated using different contact force sequences, *i.e.* varying the contact force from low-to-high values (0 to 45 nN), from high-to-low values (45 to 0 nN), and using randomly selected alternate forces. In all cases, the depth values are repeatable, indicating the reliability and reproducibility of the data in Fig. 3; and (iii) the observation of low depths using low contact forces (~ 250 nm at 4.5 nN) after high depths using high contact forces (~ 950 nm at 45 nN) con-

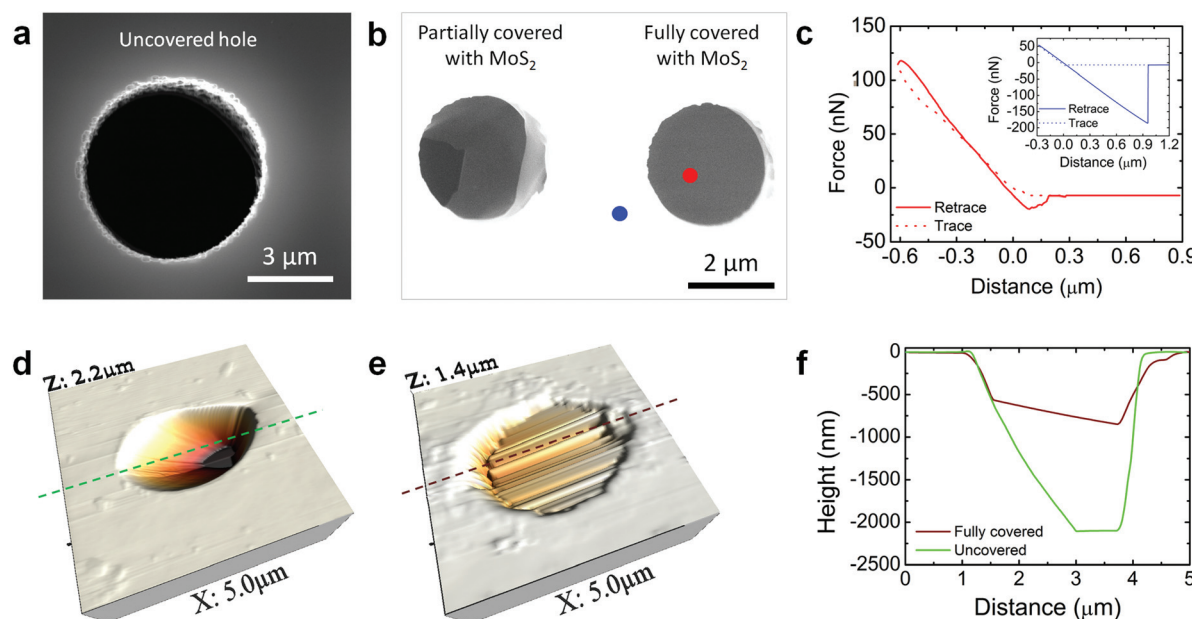


Fig. 2 SEM images of (a) an uncovered hole and (b) two holes partially and fully covered by MoS₂. (c) Force distance (F-d) curve collected on the MoS₂-covered hole and on Si (inset). The points where the F-d curves are collected are highlighted in (b) with red/blue dots. On Si (blue dot) the F-d curve follows the typical shape on rigid substrates, but on the MoS₂-covered hole (red dot) the shape is not straight, indicating that the MoS₂ membrane is suspended. (d) and (e) AFM maps of an uncovered and fully covered hole (respectively). (f) Cross sections of (d) and (e) at the dashed lines.

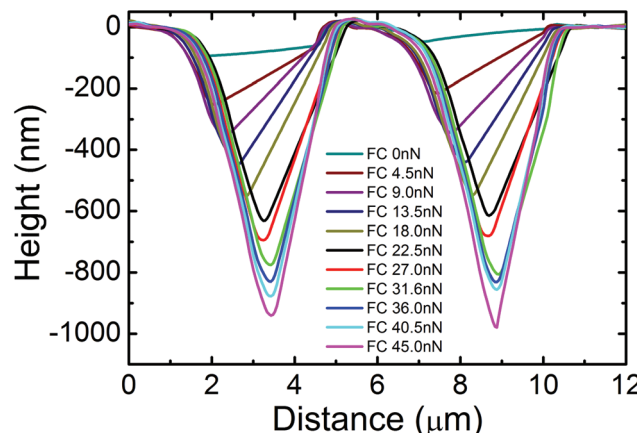


Fig. 3 Cross sections in AFM topographic maps of suspended MoS₂ using different forces. The graph shows the progressive increase of depth with the contact force. The asymmetric shape at low contact forces is related to the direction of the scan (see also Fig. S4 in the ESI†).

firms the relaxation of the strain in the flakes, and eliminates the possibility of sliding inside the hole. Similar experiments were previously reported for MoS₂³⁸ and other LMs,³⁹ with equivalent results. Therefore, Fig. 3 corroborates that the flakes are strained for contact forces ranging between 0 and 45 nN.

As ML-MoS₂ flakes have shown to be piezoelectric,¹⁹ the strained flakes in Fig. 3 should generate a potential between different points. We note that different orientations of mechanical strain may generate currents in different directions. Ref. 19 observed that mechanical strains applied in the ‘armchair’

and ‘zig-zag’ directions generate currents of opposite polarities. Ref. 3 reported that a vertical force applied with an AFM tip at the center of MoS₂ flakes generates a net ring-like field in the tip/MoS₂ system, with the positive potential at the tip and the negative at the surroundings. To confirm these results, the experiments in Fig. 3 are then repeated using conductive AFM tips, and the current is monitored with varying contact force (22–247 nN). Fig. 4a shows that, in the absence of bias, large (~150 pA) currents can be measured on the strained MoS₂ membrane suspended on the hole (indicated with a dotted circle), and no current is observed on the bare n⁺⁺-Si (out of the hole). The propagation of the current outside the hole at high contact forces indicates that the MoS₂ flakes may have been folded at that position, a behavior already known when scanning a LM surface with an AFM tip.^{33,40} In any case, the observation of currents above 150 pA without bias only at the strained areas corroborates the presence of piezoelectric effects, as it was similarly observed in both LMs¹⁹ and nanowires.¹² Ref. 41 reported that a pressure induced semiconductor-to-metal transition can be expected in MoS₂ flakes, with an induced structural phase transfer from the original 2H_c to 2H_a-MoS₂. Ref. 41 identified three characteristic regions under different contact forces: (i) below 10 GPa, MoS₂ behaves as a semiconductor; (ii) between 10 and 19 GPa, an intermediate state is reached; (iii) and above 19 GPa, the material behaves as a metal. In our experiments the contact force applied with the tip of the CAFM is limited by the length of the cantilever and the deflection setpoint used, and the maximum we applied is 247 nN (see Fig. 4a). As in CAFM experiments the tip/sample contact area is typically 100 nm²

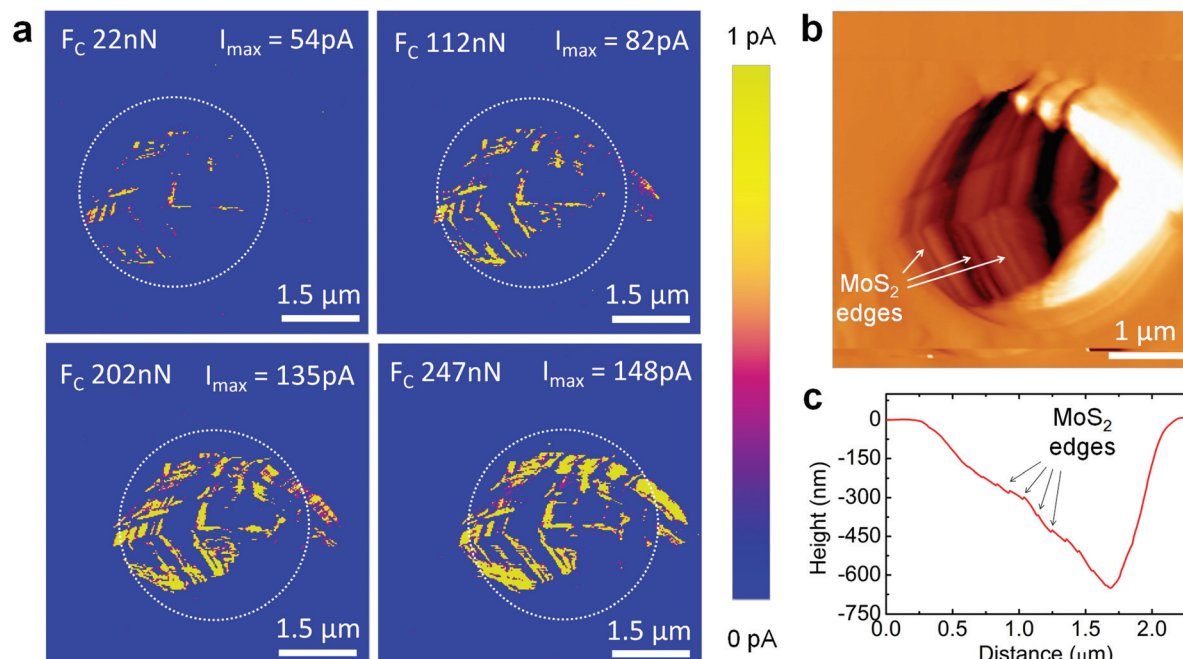


Fig. 4 (a) Current AFM maps measured for different contact forces, showing an increase of current. The dashed circles indicate the location of the hole. (b) Derivative of the topographic map collected simultaneously to panel (a). The image shows multiple steps. (c) Cross section of a topographic map collected on the hole. The image displays the ML nature of the suspended MoS₂ flake.

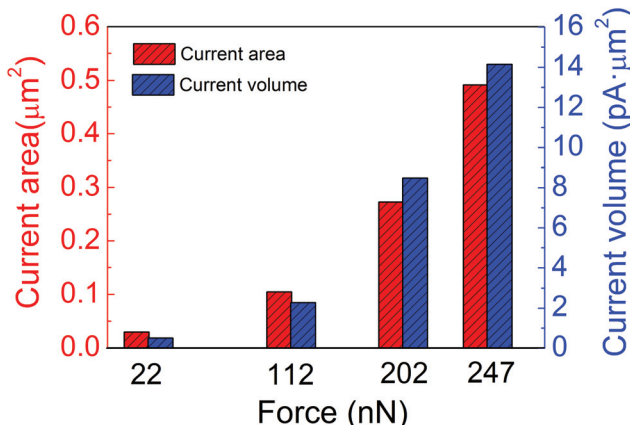


Fig. 5 The total area and volume of the current spots for the maps collected using forces of 22 nN, 112 nN, 202 nN and 247 nN (displayed in Fig. 4a). Both magnitudes increase with the contact force.

that gives a pressure of 2.47 GPa, which ensures that we are working within the region of semiconducting character.⁴¹ Therefore, we do not consider the larger currents observed here as a consequence of phase transition or band structure modification in MoS₂. Furthermore, although a strain gradient is induced with the CAFM tip, the observation of current cannot be attributed to the flexoelectric effect, which is negligible in MoS₂ flakes.⁴² The total area and volume of the currents generated have been quantified using the WSxM software of the AFM,⁴³ and a relationship with the contact force can be observed in Fig. 5, further supporting the link between mechanical strain and current. Note that, in CAFM experiments, an increase of contact force (F_c) usually produces an increase of the tip/sample contact area (A_c),⁴⁴ which may raise the currents registered, as $I = J \cdot A_c$ (where I is the total current measured by the CAFM and J is the current density). Nevertheless, this effect cannot explain the observations of current generation in Fig. 4 and 5, as they are obtained without bias, and would imply $J \sim 0$. In other words, the tip/

sample contact area effect can explain small current increases (few picoamperes in the presence of bias), but not the large (~150 pA) currents generated in the absence of bias. The currents in Fig. 4 are reproducible using both contact mode CAFM and Peak Force TUNA,⁴⁵ which measures the current in dynamic tapping mode, discarding the effect of parasitic static currents.

The current maps reveal that the areas of the MoS₂ flakes that show large currents follow a correlation with the topographic profile, as displayed in Fig. 4b and c. On the areas with flat morphology the density of current spots is smaller, while regions full of steps are more active. This behavior can be further analyzed via small area (250 nm × 250 nm) scans. Fig. 6a plots the deflection error map collected at a stepped location of the sample. This image is especially interesting because it displays steps in the MoS₂ better than the topographic map. Fig. 6b shows the simultaneously collected current map in the absence of bias. The images reveal a good correlation (see also Fig. S5 in the ESI†), indicating that the steps in the ML flakes are genuine features promoting the generation of current. The superior piezoelectric effect at the edges could be related to an increased asymmetry due to the exposed S atoms at the edges, as well as the increased density of electrons, which enhances charge transport.^{46,47} This is consistent with the observation that taller steps show larger currents (as seen in Fig. 6a and b), because they should contain a larger amount of vacancies, which favor asymmetries in the film and the generation of piezoelectricity. The areas in Fig. 6b that show no current (*i.e.* small steps and plateaus) may be driving currents below the resolution of the CAFM (this setup can only detect currents above 1 A cm⁻²). In the case of plateaus, currents are less likely to be generated due to non-optimal crystal orientation with respect to the tip.¹⁹ Fig. 6c superimposes topographic and current cross-sections, which show a step/current correlation. Other special properties related to the exposed atoms at the edges of MoS₂ sheets were previously reported. Ref. 48 theoretically predicted that the edges of MoS₂ may promote the disassociation of water by

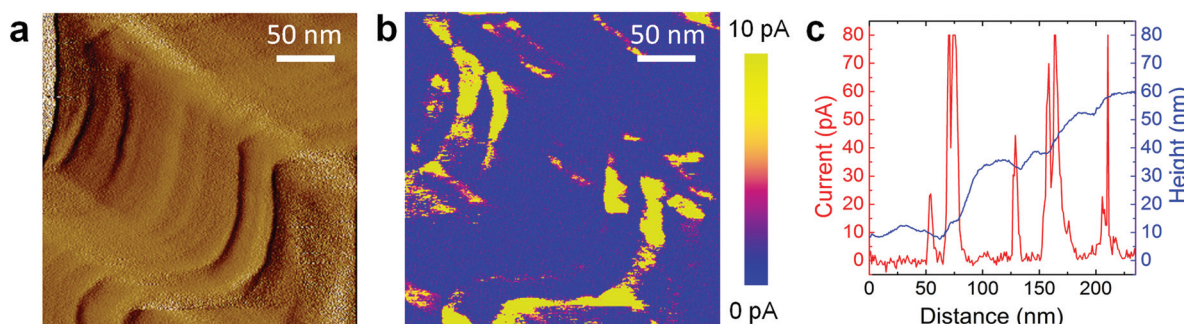


Fig. 6 (a) Deflection error map collected in a random location of suspended MoS₂ (inside the hole) without bias. This image displays the features of the topography, and the flake edges. (b) Current map collected simultaneously to (a), and therefore with zero bias, showing that the current is mainly concentrated at the flake edges. The vertical scale of (a) is in arbitrary units, and the one of (b) is: blue 0 pA and yellow 10 pA. As the tip/sample contact area in CAFM experiments is typically ~100 nm², the current densities measured in (b) exceed 10 A cm⁻². (c) Overlapped cross section of a topographic and a current map collected simultaneously on suspended MoS₂, showing the correlation between steps and current peaks.

covalent bonding of oxygen and hydrogen at its zigzag and armchair edges. These hypotheses were experimentally demonstrated in ref. 46, where the electrocatalytic hydrogen evolution reaction was observed at the edges of 1L-MoS₂ flakes.

The absence of current observed with the CAFM at the flat areas of the MoS₂ nanosheets (at the plateaus, out of the edge region, see Fig. 6b and c) is not in conflict with the previous demonstrations of piezoelectricity at MoS₂ sheets with an odd N.^{18,19} The reason is that the minimum current density that a standard CAFM can map is $\sim 1 \text{ A cm}^{-2}$ (1 pA flowing through an area of $\sim 100 \text{ nm}^2$). Therefore, the current densities generated at the plateaus (if any) are below 1 A cm^{-2} , while the edges in the MoS₂ generate current densities above that value, both at regions with an even and odd N. In fact, in our experiments it is complex determine N at each location, but we clearly observe that the piezocurrents are generated at all the edges (no spatial alternation is observed, see Fig. 6b and c).

In order to gain further insights, we perform density functional theory (DFT) calculations. Two structures are considered, (1) a single 1L-MoS₂ deformed with a circular indent (see Fig. 7a) to simulate the physical case depicted in Fig. 2e, and (2) a stepped trilayer (3L) MoS₂ (see Fig. 7c and d) to mimic the experimentally observed steps in Fig. 4 and 6. As it is not feasible to perform DFT calculations on the micrometer scale of the experiments, we model similar systems with smaller dimensions (as commonly done in DFT studies).⁴⁹ Because DFT calculations scale as cube of the number of atoms, if the size of the system is doubled (number of atoms) the calculation takes 8 times as long. To go to larger systems one would need to sacrifice the accuracy of the calculations (tight-binding or a classical model). More specifically, for structure (1) we construct a $4.4 \text{ nm} \times 3.8 \text{ nm}$ MoS₂ sheet. To mimic the deformation due to the CAFM tip, we displace the central atoms of the MoS₂ sheet along the vertical axis (see

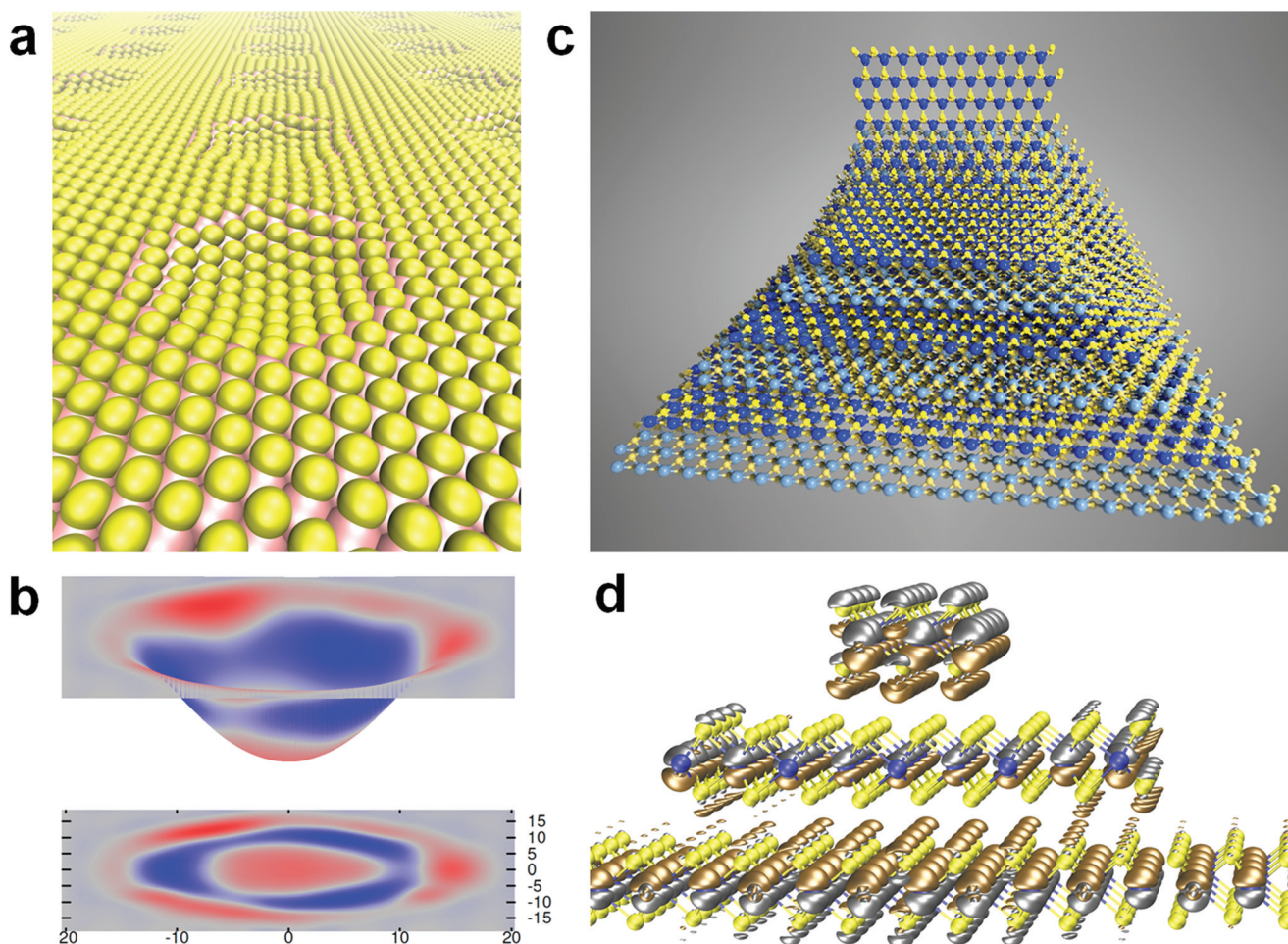


Fig. 7 (a) Atomic structure of a 1L-MoS₂ deformed to represent the experiments: yellow spheres S, pink spheres Mo. The strain-induced charge separation is shown in (b). The different colours indicate the amount of excess or missing charge on each atomic site in units of electron charge. Red colour corresponds to a negative charge accumulation of 0.015, grey is zero and blue indicates a positive charge accumulation of 0.015. The colour map is projected onto the X-Y plane for additional perspective. (c) Illustration of a ML-MoS₂ sheet with a stepped structure, in which both the hexagonal lattice of the MoS₂ sheet and the edges can be distinguished. For clarity, even and odd layers have been coloured with different tonalities. (d) DFT simulation of a 3L-MoS₂ edge showing an accumulation of excess electron charge density at the edges (silver lobes) upon stretching along the step direction.

Fig. 7a). This deformed circular pattern in the center of the 1L-MoS₂ has a diameter of ~2.8 nm. The ratio between the diameter and vertical deformation (D/L) is consistent with the experiments. The atoms outside the circular region, which represent the portion of MoS₂ supported by the substrate, are initially given positions corresponding to an unstrained 1L-MoS₂. Periodic boundary conditions are employed in all directions and periodically replicated MoS₂ layers are separated by 2 nm in the vertical direction, sufficient to eliminate any interaction between neighboring sheets.

Holding the positions of the Mo atoms fixed in this deformed shape, all coordinates of the S atoms are allowed to relax to the lowest energy configuration under the deformation constraint. We then obtain the Löwdin charges^{50,51} (*i.e.* the projections of the electron density onto orthonormalized atomic orbitals) on each atomic site. The partial Löwdin charges are used in Fig. 7b to plot the response of the electric charge of a single 1L-MoS₂ to the deformation induced by the AFM tip when pushing on the center of the suspended region. No charge separation occurs in the unperturbed flat region, as expected (gray color). Within the depressed region, a net negative charge accumulates around the rim of the circular depression and at the center of the indentation (red colors), while a compensating net positive charge appears in a ring pattern between the rim and the center (blue). A three-fold symmetry is evident in the charge distribution, following the symmetry of the crystal lattice. This result agrees with the direction of the electrical field reported by Ref. 3 and further supports the generation of a ring-like electric field in the tip/MoS₂ system. These calculations use an energy convergence threshold of 10^{-7} eV.

Turning to structure (2), we find that the enhanced piezoelectric effect at the step edges is also predicted by DFT. Fig. 7d shows a 3L-MoS₂ formed into a step structure with the steps terminated in the 'zig-zag' pattern. This model also employs periodic boundary conditions in each direction. The ground-state electronic charge density is obtained for two cases: (i) the structure relaxed to the experimental lattice parameters, and (ii) the structure relaxed after the lattice parameter is stretched by 2% along the step direction. The isosurfaces in Fig. 7d show the change in charge density due to this stretching. Excess electron charge density accumulates along the top of the highest step and the top of the edges of the middle step (silver lobes) while electron density is lost from the underside of these steps (brown lobes). There is little electron density difference at the surface of the bottom sheet. These results are consistent with the observation of increased scanning tunneling microscopy current at the step edges of the stretched sheets.⁵²

In summary, the piezoelectric properties of liquid-phase exfoliated MoS₂ have been mapped with nanoscale precision. Our experiments demonstrate the generation of currents with no need of bias, when the MoS₂ flakes are strained. Further, the current increases with the applied force. The lateral resolution of this technique allowed us to map the features that promote piezoelectricity. The edges in ML-MoS₂ membranes

show the largest currents, up to 148 pA ($J = 148 \text{ A cm}^{-2}$). These results can have implications in printable electronics, with applications including self-powered devices, sensors, transformers and antennas.

Methods

Piezoelectric effect characterization

In order to characterize the properties of the MoS₂ flakes at the nanoscale, we fabricate a substrate with matrices of holes patterned so that the flakes can be suspended and strained with the CAFM tip. We use phosphorus-doped n-type silicon wafers ($n^{++}\text{-Si}$) with a resistivity of (0.05–0.1 Ω cm) from Suzhou Research Semiconductor Co. Ltd. Matrices of holes with different diameters ranging between 2 and 6 μm are patterned by Inductively Coupled Plasma Reactive Ion Etching (ICP-RIE). The depth of the holes is 2.2 μm , and each matrix is numbered so that different experiments could be conducted on the same site.

The presence of MoS₂ across the holes is verified with a Zeiss SUPRA55 Scanning Electron Microscope (SEM). The morphology is analyzed with a Veeco Multimode VAFM working in tapping mode and using silicon tips from NanoWorld (model NCH, item no. 78131F6L965). The piezoelectric effect is characterized by current maps obtained in contact mode with the conductive module of the same AFM. Additional electrical information is recorded using the Peak Force TUNA mode of a Multimode VIII AFM. For the electrical measurements we use metal-varnished silicon tips from Bruker (model SCM-PIC item no. A009/07-07/14, and SNL-10 item no. A044/09-04/13). The metallic varnish of the SCM-PIC and SNL-10 tips is Pt–Ir and Ti–Au, respectively. The nominal spring constant and resonant frequency of SCM-PIC tips are 0.2 N m⁻¹ and 13 kHz, respectively. Similarly, for the SNL-10 tips the values of these two parameters are 0.12 N m⁻¹ and 23 kHz. The parameters used for collecting the current maps are as follows: DC sample bias = 0 V; preamplifier gain = 10^9 ; sensitivity = 1 nA V⁻¹. The data collected were of current (ampères unit). A preamplifier with a gain 10^9 implies a load resistance of 1 G Ω , which is of the same order of magnitude as that used in other studies.¹⁰ The AFM images are processed with two different AFM softwares: Nanoscope Analysis 1.40 from Bruker and WSxM (version 5.0 develop 7.0) from Nanotech.

Density functional theory calculations

DFT calculations are done with the Quantum espresso code⁵³, using Projector Augmented Wave (PAW) atomic datasets,^{54,55} the Perdew–Burke–Ernzerhof Generalized Gradient Approximation (PBE/GGA) exchange correlation functional,⁵⁶ a 30 Ry cut-off energy for the wave functions and a 240 Ry kinetic energy cut-off for the charge density, and an energy convergence threshold of 10^{-8} Ry. Calculations for structure (1) use Γ -point sampling of reciprocal space, while the calculations for structure (2) sample 5 points in the direction paral-

lel to the step edges ($5 \times 1 \times 1$ k -point sampling). Both structures employed periodic boundary conditions as noted above.

Acknowledgements

We acknowledge funding from the Young 1000 Global Talent Recruitment Program of the Ministry of Education of China (KG and ML), the National Natural Science Foundation of China (grants no. 61502326, 41550110223, 11661131002, 11375127), the Jiangsu Government (grant no. BK20150343, BK20130280), the Ministry of Finance of China (grant no. SX21400213), the Young 973 National Program of the Chinese Ministry of Science and Technology (grant no. 2015CB932700) and the ERC Grant Hetero2D, the EU Graphene Flagship, EPSRC Grants EP/K01711X/1, EP/K017144/1, EP/L016087/1, EP/N010345/1, the Collaborative Innovation Center of Suzhou Nano Science & Technology, the Jiangsu Key Laboratory for Carbon-Based Functional Materials & Devices and the Priority Academic Program Development of Jiangsu Higher Education Institutions.

References

- 1 H. Fu and R. E. Cohen, *Nature*, 2000, **403**, 281.
- 2 T. Wu and H. Zhang, *Angew. Chem., Int. Ed.*, 2015, **54**, 4432.
- 3 J. J. Qi, Y. W. Lan, A. Z. Stieg, J. H. Chen, Y. L. Zhong, L. J. Li, C. D. Chen, Y. Zhang and K. L. Wang, *Nat. Commun.*, 2015, **6**, 7430.
- 4 X. D. Wang, J. Zhou, J. Song, J. Liu, N. S. Xu and Z. L. Wang, *Nano Lett.*, 2006, **6**, 2768.
- 5 O. Lopez-Sanchez, D. Lembke, M. Kayci, A. Radenovic and A. Kis, *Nat. Nanotechnol.*, 2013, **8**, 497.
- 6 N. Elvin, A. Elvin and D. H. Choi, *J. Strain Anal. Eng. Des.*, 2003, **38**, 115.
- 7 H. A. Sodano, *J. Intell. Mater. Syst. Struct.*, 2005, **16**, 799.
- 8 H. J. Xiang, J. L. Yang, J. G. Hou and Q. S. Zhu, *Appl. Phys. Lett.*, 2006, **89**, 223111.
- 9 B. Xiang, P. G. Wang, X. Z. Zhang, S. A. Dayeh, D. P. Aplin, C. Soci, D. Yu and D. Wang, *Nano Lett.*, 2007, **7**, 323.
- 10 Z. L. Wang and J. H. Song, *Science*, 2006, **312**, 242.
- 11 S. Xu, Y. Qin, C. Xu, Y. G. Wei, R. S. Yang and Z. L. Wang, *Nat. Nanotechnol.*, 2010, **5**, 366.
- 12 M. Lanza, M. Reguant, G. J. Zou, P. Y. Lv, H. Li, R. Chin, H. Y. Liang, D. P. Yu and H. L. Duan, *Adv. Mater. Interfaces*, 2014, **1**, 1300101.
- 13 S. Hu, C. Y. Chi, K. T. Fountaine, M. Yao, H. A. Atwater, P. D. Dapkus, N. S. Lewis and C. Zhou, *Energy Environ. Sci.*, 2013, **6**, 1879.
- 14 K. H. Michel and B. Verberck, *Phys. Rev. B: Condens. Matter*, 2011, **83**, 115328.
- 15 M. T. Ong and E. J. Reed, *ACS Nano*, 2012, **6**, 1387.
- 16 K. E. El-Kelany, P. Carbonnière, A. Erba and M. Rérat, *J. Phys. Chem. C*, 2015, **119**, 8966.
- 17 K.-A. N. Duerloo, M. T. Ong and E. J. Reed, *J. Phys. Chem. Lett.*, 2012, **3**, 2871.
- 18 H. Y. Zhu, Y. Wang, J. Xiao, M. Liu, S. M. Xiong, Z. J. Wong, Z. L. Ye, Y. Ye, X. B. Yin and X. Zhang, *Nat. Nanotechnol.*, 2015, **10**, 151.
- 19 W. Wu, L. Wang, Y. L. Li, F. Zhang, L. Lin, S. Niu, D. Chenet, X. Zhang, Y. Hao, T. F. Heinz, J. Hone and Z. L. Wang, *Nature*, 2014, **514**, 470.
- 20 S. Manzeli, A. Allain, A. Ghadimi and A. Kis, *Nano Lett.*, 2015, **15**, 5330.
- 21 H. Wang, H. B. Feng and J. H. Li, *Small*, 2014, **10**, 2165.
- 22 A. C. Ferrari, F. Bonaccorso, V. Fal'ko, K. S. Novoselov, S. Roche, P. Bøggild, S. Borini, F. H. Koppens, V. Palermo, N. Pugno, J. A. Garrido, R. Sordan, A. Bianco, L. Ballerini, M. Prato, E. Lidorikis, J. Kivioja, C. Marinelli, T. Ryhänen, A. Morpurgo, J. N. Coleman, V. Nicolosi, L. Colombo, A. Fert, M. Garcia-Hernandez, A. Bachtold, G. F. Schneider, F. Guinea, C. Dekker, M. Barbone, Z. Sun, C. Gallois, A. N. Grigorenko, G. Konstantatos, A. Kis, M. Katsnelson, L. Vandersypen, A. Loiseau, V. Morandi, D. Neumaier, E. Treossi, V. Pellegrini, M. Polini, A. Tredicucci, G. M. Williams, B. H. Hong, J. H. Ahn, J. M. Kim, H. Zirath, B. J. van Wees, H. van der Zant, L. Occhipinti, A. Di Matteo, I. A. Kinloch, T. Seyller, E. Quesnel, X. Feng, K. Teo, N. Rupesinghe, P. Hakonen, S. R. Neil, Q. Tannock, T. Löfwander and J. Kinaret, *Nanoscale*, 2015, **7**, 4598.
- 23 S. Chandratre and P. Sharma, *Appl. Phys. Lett.*, 2012, **100**, 023114.
- 24 M. Yi and Z. G. Shen, *J. Mater. Chem. A*, 2015, **15**, 5330.
- 25 J. N. Coleman, M. Lotya, A. O'Neill, S. D. Bergin, P. J. King, U. Khan, K. Young, A. Gaucher, S. De, R. J. Smith, I. V. Shvets, S. K. Arora, G. Stanton, H.-Y. Kim, K. Lee, G. T. Kim, G. S. Duesberg, T. Hallam, J. J. Boland, J. J. Wang, J. F. Donegan, J. C. Grunlan, G. Moriarty, A. Shmeliov, R. J. Nicholls, J. M. Perkins, E. M. Grieveson, K. Theuwissen, D. W. McComb, P. D. Nellist and V. Nicolosi, *Science*, 2011, **311**, 568.
- 26 A. O'Neill, U. Khan and J. N. Coleman, *Chem. Mater.*, 2012, **24**, 2414.
- 27 F. Bonaccorso, A. Lombardo, T. Hasan, Z. Sun, L. Colombo and A. C. Ferrari, *Mater. Today*, 2012, **15**, 564.
- 28 F. Torrisi, T. Hasan, W. Wu, Z. Sun, A. Lombardo, T. S. Kulmala, G.-W. Hsieh, S. Jung, F. Bonaccorso and P. J. Paul, *ACS Nano*, 2012, **6**, 2992.
- 29 S. Agarwal and E. Yablonovitch, *Nano Lett.*, 2014, **14**, 6263.
- 30 D. Sinha and G. A. J. Amaralunga, *Phys. Rev. Lett.*, 2015, **114**, 147701.
- 31 Website of Graphene Supermarket (MoS₂ Solution) <https://graphene-supermarket.com/MoS2-Pristine-Flakes-in-Solution.html>.
- 32 U. Khan, A. O'Neill, M. Lotya, S. De and J. N. Coleman, *Small*, 2010, **6**, 864–871.
- 33 C. Lee, H. Yan, L. E. Brus, T. F. Heinz, J. Hone and S. Ryu, *ACS Nano*, 2010, **4**, 2695.
- 34 N. Wakabayashi, H. G. Smith and R. M. Nicklow, *Phys. Rev. B: Solid State*, 1975, **12**, 659.

- 35 P. Nemes-Incze, Z. Osvath, K. Kamaras and L. P. Biro, *Carbon*, 2008, **46**, 1435.
- 36 S. Z. Butler, S. M. Hollen, L. Y. Cao, Y. Cui, J. A. Gupta, H. R. Gutiérrez, T. F. Heinz, S. S. Hong, J. X. Huang, A. F. Ismach, E. Johnston-Halperin, M. Kuno, V. V. Plashnitsa, R. D. Robinson, R. S. Ruoff, S. Salahuddin, J. Shan, L. Shi, M. G. Spencer, M. Terrones, W. Windl and J. E. Goldberger, *ACS Nano*, 2013, **7**, 2898.
- 37 Y. Y. Shi, Y. F. Ji, H. Sun, F. Hui, J. C. Hu, Y. X. Wu, J. L. Fang, H. Lin, J. X. Wang, H. L. Duan and M. Lanza, *Sci. Rep.*, 2015, **5**, 11232.
- 38 S. Bertolazzi, J. Brivio and A. Kis, *ACS Nano*, 2011, **5**, 9703.
- 39 C. Lee, X. D. Wei, J. W. Kysar and J. Hone, *Science*, 2008, **321**, 385.
- 40 C. G. Lee, Q. Y. Li, W. Kalb, X. Z. Liu, H. Berger, R. W. Carpick and J. Hone, *Science*, 2010, **2**, 328.
- 41 A. P. Nayak, S. Bhattacharyya, J. Zhu, J. Liu, X. Wu, T. Pandey, C. Jin, A. K. Singh, D. Akinwande and J. F. Lin, *Nat. Commun.*, 2014, **5**, 3731.
- 42 J. Zhang, C. Wang and C. Bowen, *Nanoscale*, 2014, **6**(22), 13314.
- 43 I. Horcas, R. Fernández, J. M. Gómez-Rodríguez, J. Colchero, J. Gómez-Herrero and A. M. Baro, *Rev. Sci. Instrum.*, 2007, **78**, 013705.
- 44 M. Lanza, M. Porti, M. Nafría, X. Aymerich, E. Whittaker and B. Hamilton, *Rev. Sci. Instrum.*, 2010, **81**, 106110.
- 45 Website of bruker (section Peak force tuna). <https://www.bruker.com/cn/products/surface-and-dimensional-analysis/atomic-force-microscopes/modes/modes/peakforce-modes.html>.
- 46 J. Benson, M. Li, S. B. Wang and P. Wang, *ACS Appl. Mater. Interfaces*, 2015, **7**, 14113.
- 47 W. J. Zhang, C. P. Chuu, J. K. Huang, C. H. Chen, M. L. Tsai, Y. H. Chang, C. T. Liang, Y. Z. Chen, Y. L. Chueh, J. H. He, M. Y. Chou and L. J. Li, *Sci. Rep.*, 2014, **4**, 3826.
- 48 K. K. Ghuman, S. Yadav and C. V. Singh, *J. Phys. Chem. C*, 2015, **119**, 6518.
- 49 E. L. Rosen, K. Gilmore, A. M. Sawvel, A. T. Hammack, S. E. Doris, S. Aloni, V. Altoe, D. Nordlund, T.-C. Weng, D. Sokaras, B. E. Cohen, J. J. Urban, D. F. Ogletree, D. J. Milliron, D. Prendergasta and B. A. Helms, *Chem. Sci.*, 2015, **6**, 6295.
- 50 P.-O. Löwdin, *J. Chem. Phys.*, 1950, **18**, 365.
- 51 P.-O. Löwdin, *Adv. Quantum Chem.*, 1970, **5**, 185.
- 52 S. Helveg, J. V. Lauritsen, E. Lægsgaard, I. Stensgaard, J. K. Nørskov, B. S. Clausen, H. Topsøe and F. Besenbacher, *Phys. Rev. Lett.*, 2000, **84**(5), 951.
- 53 G. Paolo, B. Stefano, B. Nicola, C. Matteo, C. Roberto, C. Carlo, C. Davide, L. C. Guido, C. Matteo, D. Ismaila, C. Andrea Dal, G. Stefano de, F. Stefano, F. Guido, G. Ralph, G. Uwe, G. Christos, K. Anton, L. Michele, M.-S. Layla, M. Nicola, M. Francesco, M. Riccardo, P. Stefano, P. Alfredo, P. Lorenzo, S. Carlo, S. Sandro, S. Gabriele, P. S. Ari, S. Alexander, U. Paolo and M. W. Renata, *J. Phys.: Condens. Matter*, 2009, **21**, 395502.
- 54 Wake Forest University website, AOMPAW database (online available on September 15th of 2015), <http://users.wfu.edu/natalie/pwpaw/man.html>.
- 55 Quantum EXPRESSO project website, simulation database, online available on September 15th of 2015, <http://www.quantum-espresso.org/>.
- 56 J. P. Perdew, K. Burke and M. Ernzerhof, *Phys. Rev. Lett.*, 1996, **77**, 3865.